Transformative Two-Dimensional Array Configurations by Geometrical Shape-Shifting Protein Microstructures

Chee Leng Lay,[†,‡,§] Mian Rong Lee,[†,§] Hiang Kwee Lee,[†,‡] In Yee Phang,[‡] and Xing Yi Ling*[,†]

[†]Division of Chemistry and Biological Chemistry, School of Physical and Mathematical Sciences, Nanyang Technological University, Singapore 637371 and [‡]Institute of Materials Research and Engineering, Agency for Science, Technology and Research (A*STAR), 3 Research Link, Singapore 117602. [§]C.L.L. and M.R.L. contributed equally.

ABSTRACT Two-dimensional (2D) geometrical shape-shifting is prevalent in nature, but remains challenging in man-made "smart" materials, which are typically limited to single-direction responses. Here, we fabricate geometrical shape-shifting bovine serum albumin (BSA) microstructures to achieve circle-to-polygon and polygon-to-circle geometrical transformations. In addition, transformative two-dimensional microstructure arrays are demonstrated by the ensemble of these responsive microstructures to confer structure-to-function properties. The design strategy of our geometrical shape-shifting microstructures focuses on embedding precisely positioned rigid skeletal frames within responsive BSA matrices to direct their anisotropic swelling under pH stimulus. This is achieved using layer-by-layer two photon lithography, which is a direct laser writing technique capable of rendering spatial resolution in the sub-micrometer length scale. By controlling the shape, orientation and number of the embedded skeletal frames, we have demonstrated well-defined arc-to-corner and corner-to-arc transformations, which are essential for dynamic circle-to-polygon and polygon-to-circle shape-shifting, respectively. We further fabricate our shape-shifting microstructures in periodic arrays to experimentally demonstrate the first transformative 2D patterned arrays. Such versatile array configuration transformations give rise to structure-to-physical properties, including array porosity and pore shape, which are crucial for the development of on-demand multifunctional "smart" materials, especially in the field of photonics and microfluidics.

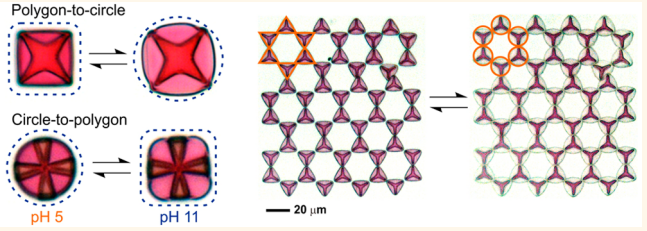

KEYWORDS: geometrical shape-shifting · two-photon lithography · bovine serum albumin · stimuli-responsive · transformative array configurations

Shape-shifting is a prevailing phenomenon in nature where organisms perform shape-to-function activities in response to external environment, including movement, structural recognition for targeted adhesion and regulation of biochemical processes.[1−4] For instance, *Amoeba proteus* undergoes multidirectional shape-shifting to form pseudopod ("false foot") for navigation and rapid path alteration.[5] Similarly, the recent advent of synthetic, micro/nanosized shape-shifting "smart" materials are also defined by their precise, dynamic and well-defined two-dimensional (2D) or three-dimensional (3D) structural change in response to stimuli.[6−13] They are applied as autonomous grippers for cargo delivery,[14−16] microactuators,[17] and microsensors.[18] These shape-shifting materials are generally limited to simple single-directional responsiveness, such as twisting,[19] bending[20] and swelling.[21] It remains a challenge to perform multiple-directional stimuli-responsiveness, which is vital for dynamic and sophisticated geometrical transformation. Such tunable and versatile geometrical feature is essential for both regulation of shape-dependent properties (such as surface area-to-volume ratio and flow characteristics) and the application in structural recognition for modulation of chemical reactivity and directing multichannel microfluidic flow.[22,23]

Furthermore, computational simulations have demonstrated that the ordered array of these dynamic, geometrical shape-shifting micro/nanosized building blocks is promising for reversible topographical change in structural configurations.[24,25] This is analogous to the self-assembly of atoms in highly symmetrical lattices,[26] where the molecular arrangement of atoms directly affect the chemical, physical and/or optical properties, such as the case of graphite and diamond.[27] To date, 2D array with

* Address correspondence to xyling@ntu.edu.sg.

Received for review April 19, 2015 and accepted September 15, 2015.

Published online September 15, 2015
10.1021/acsnano.5b04300

transformative configurations has not been realized experimentally at the submicrometer length scale. Hence, we hypothesize that both geometrical shape-shifting microstructures and their ensemble as transformative 2D patterned arrays with stimuli-responsiveness are essential for the scientific advancement of autonomous, multifunctional "smart" materials, especially for the field of photonics,[28] sensors[29] and microfluidics.[23]

Here, we demonstrate the dynamic geometrical shape-shifting of pH-responsive bovine serum albumin (BSA) microstructures from simple circles to well-defined polygons and vice versa. Moreover, 2D BSA microstructure arrays with dynamic and transformative array configurations *via* precise geometrical shape-shifting are reported. Our strategy involves layer-by-layer photoinduced polymerization of BSA to precisely modulate cross-linking density within a single protein microstructure entity at submicrometer spatial resolution. This is achieved using two-photon lithography to create region of skeletal framework (high cross-linking density) to direct swelling of low cross-linking density regions for geometrical transformation. The shape, orientation and number of the embedded skeletal frames are modulated to effect arc-to-corner and corner-to-arc transformations for various geometrical transformations. Efficacy of shape-shifting is defined by area of occupancy, radius of curvature and tangent length at edge of final transformed shapes. We then demonstrate on-demand transformation of array configurations, where protein microstructures fabricated in 2D arrays with Kagome and open-structured hexagonal configurations undergo reversible geometrical shape transformation to form hexagonal and percolating hexagonal configurations, respectively, under pH stimulus. The transformation of array configurations confers tunable structure-to-physical properties, such as array porosity and pore shape, which are crucial for future development of 2D/3D multifunctional "smart" materials.

RESULTS AND DISCUSSION

Design of Geometrical Shape-Shifting Microstructures. We achieve geometrical shape-shifting of microstructures through the spatial control of anisotropic swelling at submicrometer precision. The design involves embedding a less-responsive and highly cross-linked bovine serum albumin (BSA) segment within a responsive BSA matrix of lower cross-linking density (Scheme 1). The highly cross-linked BSA segments function as skeletal frames to induce mechanical constraints and to direct the structural anisotropic swelling of low cross-linked BSA matrix.[30−32]

The fabrication of segmented BSA microstructures with submicrometer scale spatial modulation of cross-linking density is performed using two-photon direct laser writing. Typically, laser is raster-scanned

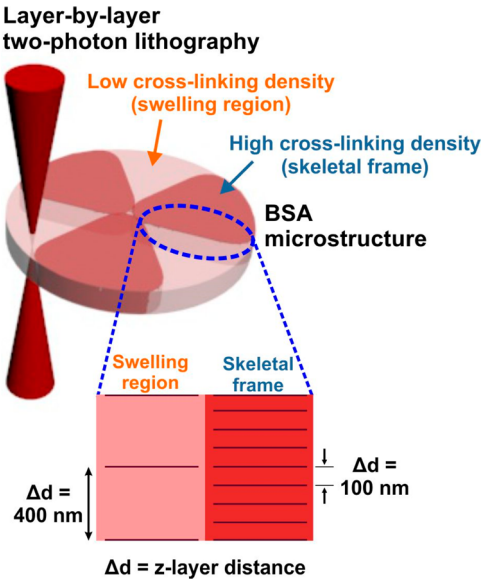

Scheme 1. Schematic of dynamic geometrical shape-shifting BSA microstructure fabricated *via* the submicrometer scaled spatial modulation of cross-linking density distribution using two-photon lithography. Z-layer distance (Δd) refers to separation between each consecutive raster-scanned $x-y$ plane during the layer-by-layer two-photon direct laser writing process.

repeatedly at a predefined $x-y$ plane to polymerize BSA resist, where the cross-linking density of the microstructure is manipulated by modulating the z-layer distance (Δd; Scheme 1) during the layer-by-layer laser writing process at submicrometer precision. Highly cross-linked BSA segments are written at Δd = 100 nm and exhibit a less-responsive swelling ratio of 1.1 on pH stimulation (Figure S1a, Supporting Information). In contrast, low cross-linked segments are written at Δd = 400 nm which allow them to swell more pronouncedly under stimulus, with a larger swelling ratio of 1.5 (Figure S1b). Hence, the cross-linking density is inversely proportional to Δd, which agrees well with literature.[33] This observation clearly demonstrates the ability of two-photon lithography to fabricate well-defined microstructures and also to precisely control the spatial distribution of cross-linking density within a microstructure.[34−36] Hereafter, BSA segments fabricated at Δd = 100 and 400 nm are termed as "skeletal frames" and "responsive BSA matrix", respectively.

Circle-to-Polygon Shape-Shifting Microstructures. For circle-to-polygon shape-shifting of BSA microstructures, the key criterion is the transformation of arc-to-corner/edge, which is critical for the generation of well-defined corners and edges of a polygon from the initial arcs of a circle (Figure 1a). Our approach lies at the induction of directed anisotropic swelling of responsive segmented BSA microstructures. We subsequently evaluate the arc-to-corner/edge transformation, and also the effectiveness of geometrical circle-to-polygon shape-shifting of our BSA microstructure using three

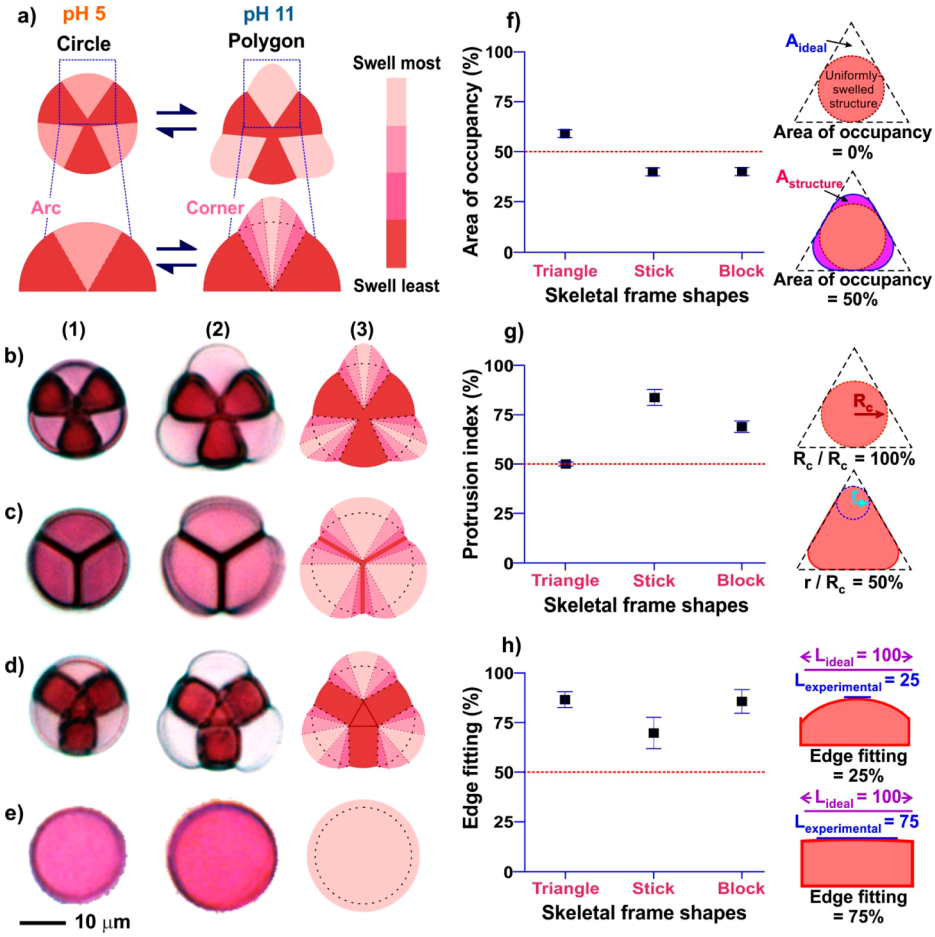

Figure 1. (a) Schematic illustrating the arc-to-corner conversions of responsive BSA matrices upon anisotropic swelling at pH 11. Circle-to-triangle shape-shifting of BSA microstructures embedded with three equally distributed (b) triangle-, (c) stick- and (d) block-shaped skeletal frames. (e) Control circular BSA microstructure in the absence of skeletal frame. (1, 2) Optical microscopic images of as-fabricated BSA microstructure at pH 5, and their transformed shape at pH 11, respectively. (3) Schematic illustrating the anisotropic swelling profile of respective BSA microstructures. Scale bar, 10 μm. Experimental comparison and schematics of (f) area of occupancy, (g) protrusion index and (h) edge fitting between shape-shifted BSA microstructures embedded with triangle-, stick- or block-shaped skeletal frames. A well-defined circle-to-polygon shape-shifting event occurs only when the transformed microstructure has area of occupancy >50%, protrusion index ≤50% and edge fitting >50%.

critical parameters, namely (1) area of occupancy, (2) protrusion index and (3) edge fitting. First, area of occupancy ($A_{structure}/A_{ideal} \times 100\%$; Figure 1f; Figure S2a,b) denotes the conformity of the swelled microstructure to the ideal intended shape which directly defines the effectiveness of geometrical shape-shifting. A_{ideal} is the area difference between a hypothetical isotropically swelled microstructure and the ideal transformed polygon; while $A_{structure}$ is the area occupied by experimental BSA microstructure within A_{ideal}. Second, protrusion index differentiates between arcs and corners and can be calculated using ($r/R_c \times 100\%$; Figure 1g; Figure S2c), where r is the radii of curvature of generated protrusions in experimentally transformed BSA microstructure and R_c is a reference radius of curvature of an isotropically swelled circular microstructure. Third, edge fitting ($L_{experimental}/L_{ideal} \times 100\%$; Figure 1h; Figure S2d) evaluates whether a microstructure's side contour resembles a straight line or an arc, which is the basis for defining an edge. Generally, we set the defining benchmark at 50% to distinguish between arc and corner, arc and edge, and to determine well-defined geometrical shape-shift from isotropically swelled microstructure (refer to Figure S2 for detailed explanations of the three parameters). A well-defined circle-to-polygon shape-shifting event therefore occurs only when the transformed microstructure has area of occupancy >50%, protrusion index ≤50% and edge fitting >50%.

Using circle-to-triangle shape-shifting as an illustration, we first embed three equally spaced triangular skeletal frames into a responsive BSA circle. When immersed in a pH 5 solution, the as-fabricated BSA microstructure remains circular due to negligible water absorption at its isoelectric point (Figure 1b(1)).[37] As the solution is changed from pH 5 to pH 11, the circular BSA microstructure becomes negatively charged and interacts strongly with water *via* ion-dipole interactions.

Consequently, the highly responsive BSA matrix undergoes anisotropic swelling directed by the skeletal frames to effect rapid circle-to-triangle shape-shifting (<2 s; Figure 1; Figure S3; Supporting Information Movie S1) *via* arc-to-corner/edge transformations, as evident from the fulfillment of the three criteria with area of occupancy being (59 ± 2)%, protrusion index (50 ± 1)% and edge fitting (87 ± 4)% (Figure 1f−h; Figure S2; Figure S4a). We attribute such anisotropic swelling to high mechanical constraints imposed by the skeletal frames. Hence, regions of responsive BSA matrix attached to or near the skeletal frame experience a greater resistance to swell (lower swelling ratio) as imposed by the stationary skeletal frame (Figure 1a; Figure 1b(3)). On the other hand, regions of the same BSA segments further away from skeletal frames are less constrained and exhibit greater swelling.[30] The presence of such a swelling gradient in the responsive BSA matrix sandwiched between two adjacent skeletal frames generates a new parabolic swelling profile. Such circle-to-triangle transformation also exhibits high reversibility on decreasing pH 11 to initial pH 5 (Figure S3).

In addition, the shape of skeletal frames has a direct impact on arc-to-corner/edge transformation and hence the precision of shape-shifting from circle-to-polygon. We demonstrate that triangular skeletal frame is superior in generating well-defined corners/edges when compared to skeletal frames of other shapes, such as sticks and blocks (Figure 1c,d). This is possibly due to sharper parabolic swelling profile generated by triangular skeletal frames (Figure 1b), which creates more oblique corners (protrusion index = 50 ± 1%; Figure S4a) than other skeletal frames of different shapes (Figure 1c,d; Figure S4b,c). As demonstrated in Figure 1c,d, BSA microstructures embedded with stick- and block-shaped skeletal frames possess broader and blunt parabolic swelling profiles due to greater separation between adjacent skeletal frames, which cannot form distinct edges and corners. BSA microstructures embedded with stick-shaped skeletal frames demonstrate area of occupancy, protrusion index, and edge fitting of (40 ± 1)%, (84 ± 4)%, and (70 ± 8)% (Figure S4b), respectively. For block-shaped skeletal frames, the parameters are quantified accordingly at (40 ± 1)%, (69 ± 3)%, and (86 ± 6)% (Figure S4c). Hence, the swelling behavior of microstructures embedded with both stick-shaped and block-shaped skeletal frames did not meet all the predefined criteria (Figure 1c,d; Figure 1f−h), and therefore, cannot be considered as successful and well-defined circle-to-triangle transformations. In comparison, a plain circular BSA microstructure with no embedded skeletal frame simply undergoes ~1.5-fold isotropic swelling at pH 11 without exhibiting shape-shifting behavior (Figure 1e). Hence, it is evident that our design in using highly cross-linked BSA skeletal frames is essential in the geometrical shape-shifting process. Hereafter, we only employ triangular skeletal frame for the fabrication of circle-to-polygon BSA microstructures due to its ability to create well-defined geometrical arc-to-corner/edge transformation.

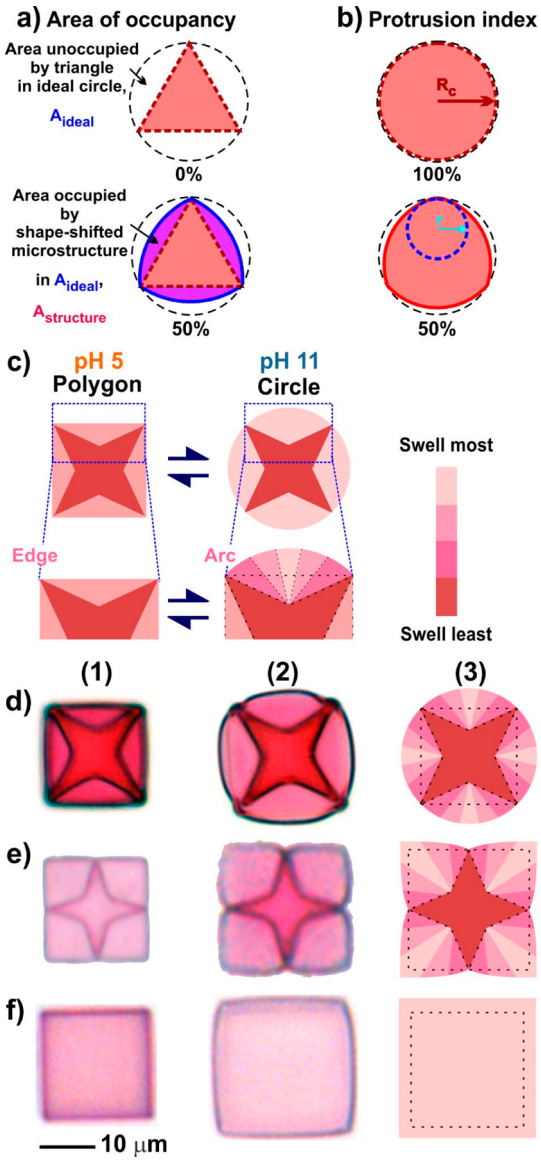

Figure 2. Schematics depicting (a) area of occupancy and (b) protrusion index to describe polygon-to-circle shape-shifting. A successful polygon-to-circle shape-shifting event occurs when area of occupancy and protrusion index are >50%. (c) Schematic illustrating the edge-to-arc conversions of responsive BSA matrices upon anisotropic swelling at pH 11. Square-to-circle shape-shifting of BSA microstructures embedded with four spike-shaped skeletal frames aligned along the (d) diagonal axes and (e) edge axes of the square. (f) Control square BSA microstructure in the absence of skeletal frame. (1, 2) Optical microscopic images of as-fabricated BSA microstructure at pH 5, and their transformed shape at pH 11, respectively. (3) Schematic illustrating the anisotropic swelling profile of respective BSA microstructures.

Polygon-to-Circle Shape-Shifting Microstructures. Our design is very versatile and is able to achieve the reverse polygon-to-circle transformation. This is attained by controlling both shape and orientation of embedded

skeletal frame within the BSA microstructure. Using similar criteria as the evaluation of circle-to-polygon transformation, we define a polygon-to-circle shape-shifting event as successful only when area of occupancy and protrusion index are >50% (Figure 2a,b; Figure S2b,c). For square-to-circle shape-shifting, we embed four spike-shaped skeletal frames in "×" arrangement in a square BSA microstructure (Figure 2d(1)). These skeletal frames are aligned along the diagonal axes of the square microstructure (oriented at 45°, 135°, 225° and 315°), with each spike bound to one of the squares' corners. This creates four regions of responsive BSA matrices, each sandwiched between two adjacent skeletal frames. As we increase pH from pH 5 to pH 11, the straight edges of the square microstructure swell anisotropically to produce arcs (Figure 2d(2)). These corner/edge-to-arc transformations drive the square-to-circle shape-shifting of BSA microstructure in <2 s with area of occupancy and protrusion index of (74 ± 8)% and (89 ± 1)%, respectively, which is also reversible on returning to pH 5 (Supporting Information Movie S2). The anisotropic swelling of responsive BSA matrix is due to pinning of skeletal frames to the four corners of the square, which restrict swelling at/near the corners. The embedded skeletal frames therefore create a broad arc-shaped swelling gradient between two adjacent corners of the square (Figure 2c; Figure 2d(3)), characterized by restricted swelling near the corners and a higher swelling ability at midpoints of the square's edges. These individual arcs generated upon swelling at pH 11 are joined at the initial corners' positions, forming the continuous arc of shape-shifted circular BSA microstructures.

The orientation of spike-shaped skeletal frames is crucial in producing well-defined polygon-to-circle transformation. We construct a similar square BSA microstructure containing spike-shaped skeletal frames but aligned along the edge's axes (oriented at 0°, 90°, 180° and 270°) instead (Figure 2e(1)). At pH 11, regions of responsive BSA matrix do not generate arcs from edges (Figure 2e(2)). Instead, it swells to yield a ~ 1.5-fold larger pinched square, which does not demonstrate geometrical shape-shifting. This observation highlights the importance of orientation-dependent anisotropic swelling of the responsive BSA matrix. When skeletal frames are aligned along the square edge's axes, a swelling gradient is created between midpoints of two edges (Figure 2e(3)). In this case, midpoints of the square edges experience the lowest swelling ability due to mechanical constraints imposed by the skeletal frame, whereas the four corners of the square exhibit highest swelling ability. As a result, the square's corners are preserved upon swelling at pH 11, leading to the formation of a larger, pinched square. Furthermore, we observe that a square BSA microstructure without skeletal frames exhibits isotropic swelling and not geometrical shape-shifting (Figure 2f). Both controls therefore

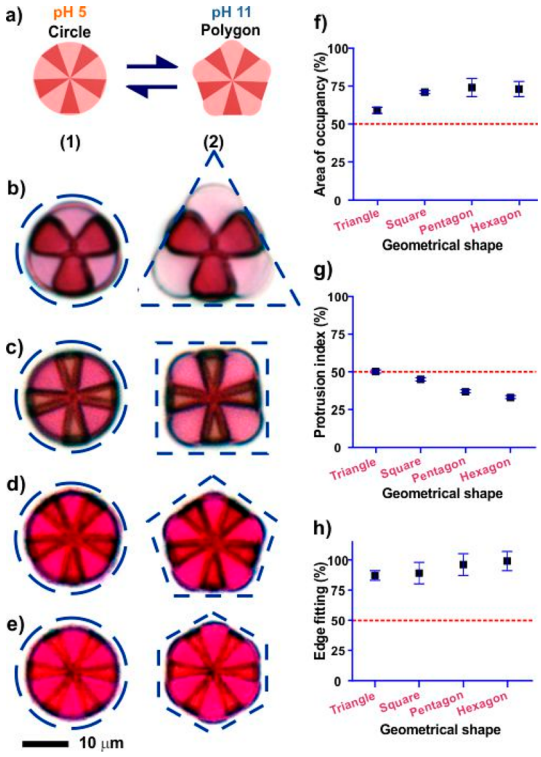

Figure 3. (a) Schematic depicting the circle-to-polygon shape-shifting of BSA microstructure on stimulation at pH 11. Optical microscopic images of dynamic geometrical shape-shifting of circular BSA microstructures to (b) triangle, (c) square, (d) pentagon, and (e) hexagon. (1, 2) Optical microscopic images of as-fabricated BSA microstructure at pH 5, and their transformed shape at pH 11, respectively. Circle-to-polygon shape-shifting efficacy expressed in terms of (f) area of occupancy, (g) protrusion index and (h) edge fitting.

clearly depict the importance of the embedded skeletal frame and its precise orientation to direct anisotropic swelling for polygon-to-circle transformation in BSA microstructures. We also determine that sharp-tipped, spike-shaped skeletal frame is essential to bind and restrict swelling near the corners effectively for generation of well-defined polygon-to-circle transformation. This is superior to blunt-tipped or stick-shaped skeletal frames, which are loosely attached to the polygon's corners and do not yield geometrical shape-shifting to circle effectively (area of occupancy = 223 ± 7% and protrusion index = 50 ± 8%; Figure S5b).

Generation of a Library of Geometrical Shape-Shifting Microstructures. On the basis of our design strategy above, we fabricate a library of circle-to-polygon shape-shifting BSA microstructures. The quantity of embedded triangular skeletal frames is controlled to enforce the essential arc-to-corner transformations in the responsive BSA matrix. We embed four, five and six equally spaced triangular skeletal frames in circular BSA microstructures (Figure 3c–e) to create square, pentagon and hexagon from circle at pH 11, respectively. This is attributed to the precise generation of four, five and six corners as a result of the anisotropic swelling of

responsive BSA matrix sandwiched between skeletal frames (Figure S6; Supporting Information Movie S3). We observe that the shape-shifted triangle, square, pentagon and hexagon fulfill all the three criteria set for well-defined circle-to-polygon shape-shifting with area of occupancy >50%, protrusion index ≤50% and edge fitting >50% (Figure 3f−h; Figure S6−S8).

Likewise, an assortment of well-defined polygon-to-circle shape-shifting BSA microstructures are fabricated simply by embedding spike-shaped skeletal frames within responsive polygon matrices, with sharp tips of skeletal frames bound to corners of the polygons (Figure 4b−e). Using three, four, five and six spike-shaped skeletal frames, triangle, square, pentagon and hexagon BSA microstructures undergo rapid shape-shifting into circles as a result of well-defined corner/edge-to-arc conversion at pH 11, with both area of occupancy and protrusion index >50% (Figure 4; Figure S2; Figure S9 and S10; Supporting Information Movies S4, S5). Hence, it is clear that specific well-defined circle-to-polygon or polygon-to-circle transformations can be programmed by defining the number of skeletal frames embedded in the BSA microstructures.

Rules-of-Thumb for Geometrical Shape-Shifting. Collectively, we propose general rules-of-thumb for the fabrication and programming of predefined circle-to-polygon and polygon-to-circle shape-shifting into BSA microstructures. First, arc-to-corner/edge conversion is crucial in circle-to-polygon shape-shifting. This is achieved by embedding equally spaced triangle-shaped skeletal frames to direct the formation of sharp corners in circular microstructures. Second, polygon-to-circle shape-shifting requires corner/edge-to-arc transformation, which is attained by aligning the sharp tips of spike-shaped skeletal frames to polygon corners. Third, the quantity of embedded skeletal frames determines the number of regions of responsive BSA matrices available for arc-to-corner/edge or corner/edge-to-arc transitions. These general rules-of-thumb therefore highlight the versatility and simplicity of our strategy to fabricate a wide variety of programmable geometrical shape-shifting BSA microstructures. Such rapid, dynamic, well-defined and on-demand geometrical shape-shifting microstructures are essential for the future construction and study of reconfigurable "smart" materials.[24] Furthermore, our precisely engineered BSA microstructures are the first demonstration of geometrical shape-shifting, which is in contrast to conventional responsive microstructures that are typically limited to simple single-directional swelling. Such geometrical shape-shifting is essential in nature. For instance, pollen grains possess a stiff outer layer, akin to our skeletal frames, which enables their geometrical shape-shifting *via* different self-folding mechanisms to protect against dehydration.[38]

Transformative 2D Array Configurations. Next, we fabricate two transformative 2D patterned arrays with

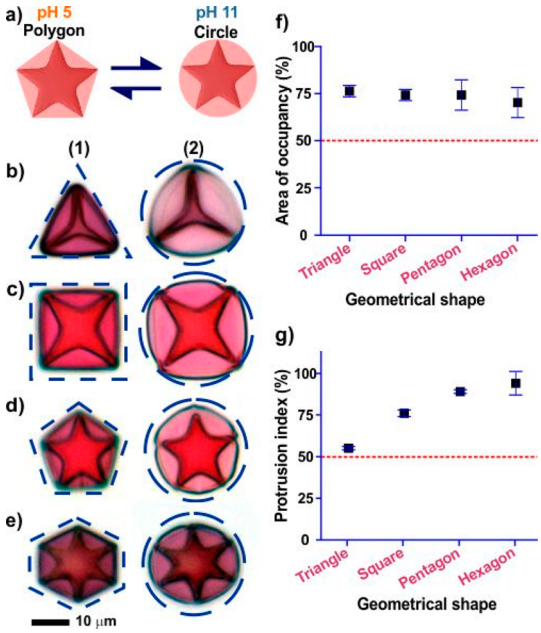

Figure 4. (a) Schematic depicting the polygon-to-circle shape-shifting of BSA microstructure on stimulation at pH 11. Optical microscopic images of dynamic shape-shifting of BSA microstructures from (b) triangle, (c) square, (d) pentagon, and (e) hexagon to circles. (1, 2) Optical microscopic images of as-fabricated BSA microstructure at pH 5, and their transformed shape at pH 11, respectively. Polygon-to-circle shape-shifting efficacy is expressed in terms of (f) area of occupancy and (g) protrusion index.

Kagome and open-structured hexagonal configurations using geometrical shape-shifting BSA microstructures and study the changes to physical properties as the array configuration transforms in response to pH stimulus. To differentiate the array configurations upon geometrical shape-shifting at pH 11, we assign "nodes" to both triangular and shape-shifted circular BSA microstructures according to their point-group symmetry, without considering the skeletal frames (Figure S11).[43] Briefly, the initial as-fabricated triangular BSA microstructure has a point group of D_{3h}, hence we allocate "nodes" at the vertices and center of microstructure to represent its D_{3h} symmetry (Figure S11a). On the other hand, circular BSA microstructure adopts point group $D_{\infty h}$ which can be in turn represented by assigning only one "node" to the center of shape-shifted circular BSA microstructure (Figure S11b).[43] The allocation of a "node" at the center of BSA microstructures is crucial to describe the position of the microstructure, which remains unchanged throughout the pH stimulation.

To start, we construct a periodic hexagonal array comprising of triangular BSA microstructures oriented outward with corner-to-corner alignment analogous of trihexagonal tiling of Kagome configuration, where each triangular microstructure represents the three vertices of a triangular tile (Figure 5a and Figure 5b(1)).[39] The "nodes" are subsequently allocated at the vertices and center of individual microstructures to

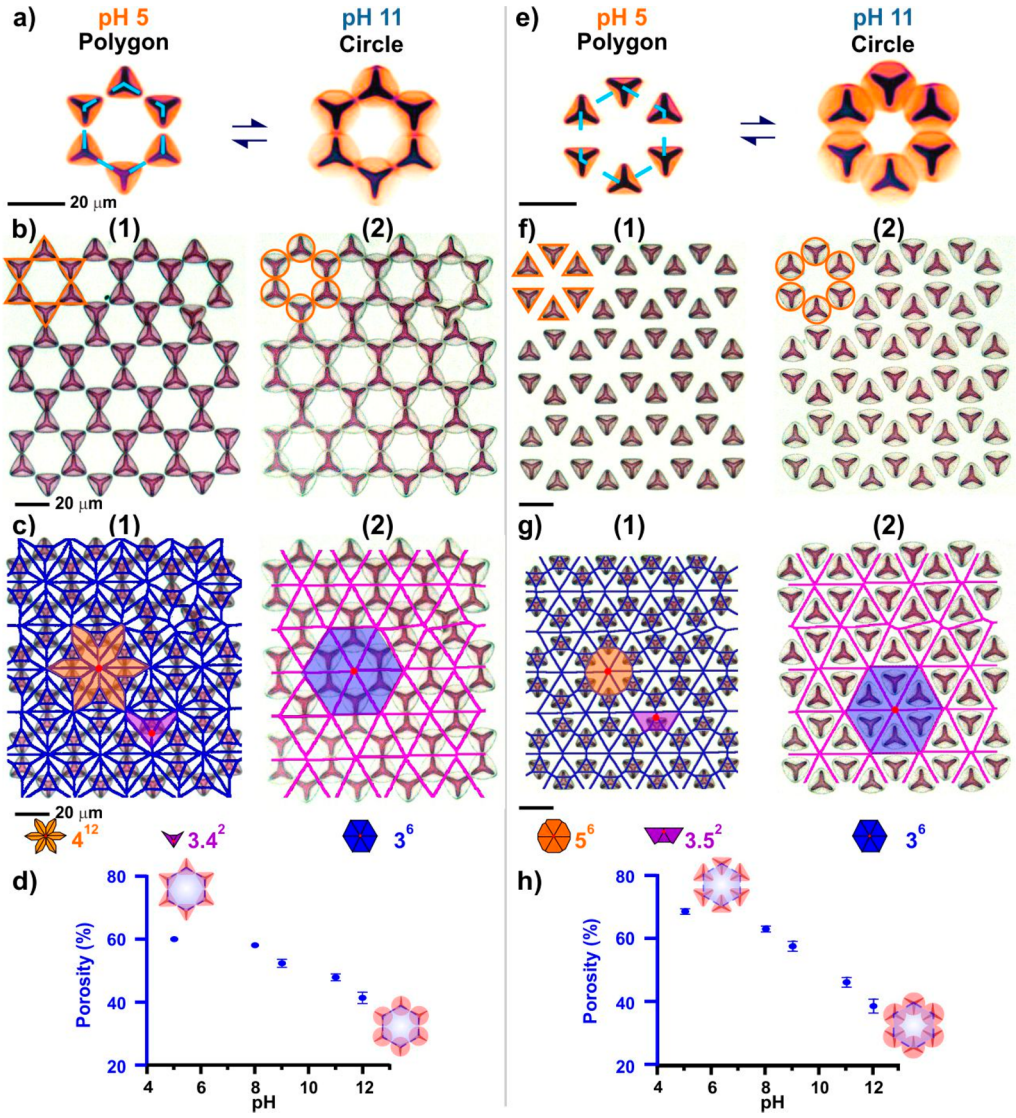

Figure 5. Raman images illustrating transformation of (a) Kagome to hexagonal and (e) open-structured hexagonal to percolating hexagonal configurations. Each Raman image uses a unit cell of six triangle-to-circle shape-shifting microstructures arranged in a hexagonal manner. Optical microscopic images depicting topographical change in array configurations during (b) Kagome to hexagonal and (f) open-structured hexagonal to percolating hexagonal array transformations. (c, g) Voronoi analysis images overlaid with the optical microscopic images of (b) and (f), respectively. (1, 2) Arrays of geometrical shape-shifting BSA microstructures at pH 5 and pH 11, respectively. Change in porosity of the two-dimesional arrays during (d) Kagome to hexagonal and (h) open-structured hexagonal to percolating hexagonal configuration transformations at different pH. All data were averaged using 10 measurements of individual unit cells and the error bars were calculated as the standard deviation from the mean.

represent their D_{3h} symmetry. The resultant configuration (Figure S12a−c) follows closely to theoretical illustrations employed in describing atomic/molecular structures of 2D materials with Kagome configuration (Figure S12g−i).[40−42] At pH 11, all individual BSA microstructures undergo triangle-to-circle transformation as both area of occupancy and protrusion index are >50%. This results in the 2D array with initial Kagome configuration morphing into a distinct hexagonal configuration made of circular microstructures, where individual circular microstructures are represented by a single "node" at their center to denote the $D_{\infty h}$ symmetry (Figure 5b(2); Figure S12e; Supporting Information Movie S6). This observation is further supported by a distinct change of tessellation in the Voronoi analysis of the reference "nodes" (Figure 5c(1−2); Figure S12), which is an image analysis method capable of visually identifying virtual network changes through forming unique tessellation by dividing the 2D space into constituting partitions.[43] We emphasize that the allocation of "nodes" should be consistent since virtual networks generated using Voronoi tessellation varies significantly with node's position caused by other arbitrary choice of similar symmetry representation for the microstructures. For Voronoi analysis on 2D array with Kagome configuration, we observe the presence of vertex types of 3.4^2 (denotes a triangle and two trapezoid-shaped faces

around a common vertex) and 4^{12} (denotes twelve trapazoid-shaped faces centered at a common vertex) (Figure 5c(1)). On the other hand, the transformed hexagonal configuration adopts a different 3^6 vertex type (denotes six triangles around a common vertex; Figure 5c(2)). The Voronoi tessellations of the experimental Kagome and hexagonal configurations obtained at pH 5 and pH 11, respectively, are comparable to their theoretical counterparts, comprising of vertex types of (3.4^2 and 4^{12}) and 3^6, respectively (Figure S12g−l). We also note that by having BSA triangular microstructures arranged in Kagome configuration (corner-to-corner alignment), the topographical change does not alter the physical connectivity of the microstructures since corner-to-corner distance remains constant (Figure 5b).

We further study the effect of Kagome-to-hexagonal configuration changes on the array porosity and pore shape, when pH is systematically tuned between pH 5−12 (Figure S13). Briefly, array porosity is the percentage of void area between BSA microstructures to the respective area of a hexagonal unit cell (Figure S13). We observe that the increment from pH 5 to pH 12 induces a transition from Kagome to hexagonal configuration. This results in both a steady decrease in array porosity from 60% to 41% (Figure 5d) and a change in pore shape from hexagon to six-pointed star (Figure S13a). Such changes to array porosity and pore shape are a consequence of triangle-to-circle shape-shifting of individual BSA microstructures with increasing pH. It is therefore evident that the physical properties of an array, such as array porosity and pore shape, can be systematically modulated upon transformation in array configurations by regulating the pH stimulus.

In addition to Kagome array configuration, we also fabricate pH-responsive and transformative 2D array with open-structured hexagonal configuration. The open-structured hexagonal array consists of inward-oriented, edge-to-edge aligned triangle-to-circle shape-shifting BSA microstructures arranged in a repeating hexagonal array, where each triangular microstructure also represents the three vertices of a triangular tile (Figure 5e and Figure 5f(1)). At pH 5, the open-structured hexagonal array exhibits Voronoi tessellation constituting of two distinct vertex types, *i.e.*, 3.5^2 and 5^6, centered at a common vertex. The 3.5^2 vertex type consists of a triangle and two diamond-shaped faces around a common vertice, whereas the vertex type of 5^6 denotes six diamond-shaped faces centered at a common vertex, respectively (Figure 5g(1); Figure S14a−c). In this example, unlike the former, the edges of the triangles approach each other as the individual BSA microstructures undergo triangle-to-circle shape-shifting (Figure 5f(2); Figure S14d−f; Supporting Information Movie S7) at pH 11, which caused the transitions of open-structured hexagonal array configuration to a percolating hexagonal configuration upon swelling. The percolating hexagonal array possesses vertex type of 3^6 in its Voronoi examination (Figure 5g(2)). This observation is in agreement with their respective theoretical Voronoi tessellation (Figure S14g−i; Figure S14j−l), which also demonstrates conversion of vertex types (3.5^2 and 5^6) to 3^6 upon transformation of array configurations. The transformation from open-structured hexagonal configuration to percolating hexagonal configuration can be attributed to the reduction in number of "nodes" which are assigned at the center of microstructures, at pH 11. This is due to the change in point group symmetries of the microstructures from D_{3h} to $D_{\infty h}$ resulting from loss of well-defined corners during the triangle-to-circle transformation of BSA microstructures as pH increases. As triangular microstructures swell into circular shape from pH 5 to pH 11, edge-to-edge distance between microstructures decreases (58 ± 4)% from (7.8 ± 0.1) μm to (3.3 ± 0.3) μm and the swollen edges approach each other (Figure S15) resulting in topological transition. The percolating hexagonal array also experiences a reduction in array porosity from 69% to 38%, while the pore shape changes from asterisk-shape to six-pointed star, the pH increases from pH 5 to pH 12 (Figure 5h; Figure S13b). With triangular BSA microstructures arranged in open-structured hexagonal array configuration, change in topology, pore shape and pore size are observed together with topographical transition from open-structured hexagonal configuration to percolating hexagonal configuration in response to pH stimulus.

Collectively, both the examples of array configuration transformations clearly exemplify the importance of our design and strategy on geometrical shape-shifting microstructures for the first experimental demonstration of dynamic, on-demand transformative 2D arrays. Together with the extensive range of transformative 2D array configurations demonstrated (Figure S16), the precise modulation of physical properties, such as connectivity and array porosity, in geometrical shape-shifting microstructure arrays marks the advent of multifunctional, tunable "smart" materials for photonic or microfluidic devices. Our work can also be extended to future studies on reconfigurable 3D crystals.

CONCLUSIONS

We have demonstrated the fabrication of a large library of well-defined circle-to-polygon and polygon-to-circle shape-shifting bovine serum albumin (BSA) microstructures by adopting three general rules-of-thumb: (1) arc-to-corner/edge conversions essential for circle-to-polygon transformation is achieved by employing triangular skeletal frames; (2) polygon-to-circle shape-shifting requires the transformation of corner/edge to arc, which is attained by orienting

spike-shaped skeletal frames toward the polygon's corners, and (3) number of corners/arcs created is controlled by the quantity of skeletal frames embedded. We apply these shape-shifting microstructures to construct the first transformative 2D array capable of undergoing reversible Kagome to hexagonal and also open-structured hexagonal to percolating hexagonal configuration transformations. Such versatile transformations in array configurations confer immense potential in the tuning of array physical properties, such as connectivity and array porosity, necessary for controlled interaction with light and fluids. This enables us to potentially tune electromagnetic wave in near-infrared region, modify fluid flow behavior and also identify and direct different phases of fluids (pH variation in this case) crucial in the field of photonics and microfluidics, respectively.[28,44−46] Our work also provides scientific insights potentially applicable for the future construction of 3D reconfigurable crystals.

METHODS

Materials. Lyophilized powdered bovine serum albumin (BSA) (96+%), HEPES (99.5+%), rose bengal (95%), powdered sodium chloride (NaCl; 99+%) and phosphate buffered saline tablets (PBS) were purchased from Sigma-Aldrich. Dimethyl sulfoxide (DMSO; AR grade), hydrochloric acid (37%), and sodium hydroxide pellet (>97%) were purchased from Goodrich Chemicals. The chemicals were used without further purification. Milli-Q water (>18.0 MΩ.cm) was purified with a Sartorius arium 611 UV ultrapure water system.

Preparation of BSA Protogel Precursor Solution. 2.9 g of BSA powder and 1.94 mL of DMSO were added to an aqueous solution of 8.5 mM rose bengal and 100 mM NaCl in 20 mM HEPES buffer to make up a total volume of 10 mL. The mixture was filtered through a hydrophilic PVDF syringe filter (pore size = 0.22 μm) to remove impurities before use.

Fabrication of BSA Microstructures. Fabrication of the protogel structures were performed using the Nanoscribe Photonic Professional. The system is equipped with a femtosecond laser source with a center wavelength of 780 nm. Structures of the protogels were designed using a CAD software, 3ds Max. Parameters of the structures were defined by the Nanoslicer and DeScribe softwares. NanoWrite software controls both the movement of piezo-driven nanopositioning scanning sample stage as well as emitting power of the laser as programmed using the Nanoslicer and DeScribe softwares. All structures were written on square glass substrates (width = 22 mm and thickness ≈0.13 to 0.16 mm) with 13 mW laser power, 0.2 μm line ($x-y$) distance, scan speed of 30 μm/s and various layer distance along z-axis (Δd). Resist containing BSA and rose bengal was deposited on a glass substrate. Photopolymerization started at the interface between resist and glass substrate, allowing fabricated structures to be firmly attached to the glass substrate. Resist within the confocal volume of the laser underwent polymerization and cross-linking on glass substrate. After fabrication, the substrate was soaked in 20 mM PBS buffer to remove excess unpolymerized resist, and subsequently washed with water and stored in nitrogen box. The fabricated microstructures remained fixed on glass substrates after development.

All individual circle-to-polygon and polygon-to-circle shape-shifting microstructures were fabricated with dimensions of 20 μm × 20 μm × 5 μm, $l \times w \times h$. Microstructures constituting the 2D patterned arrays with different configurations were fabricated with dimensions of 12 μm × 12 μm × 5 μm, $l \times w \times h$.

Dynamic Geometrical Shape-Shifting of BSA Microstructures. All as-fabricated BSA microstructures were equilibrated in pH 5 solution for 3 min and subsequently transferred to a pH 11 solution. The BSA microstructures were equilibrated for another 3 min. Both the BSA microstructures at pH 5 and pH 11 were monitored using optical microscope and Raman microscopy. For the *in situ* monitoring of shape-shifting process using optical microscope, the optical images were captured continuously as the pH of the solution was gradually increased from pH 5 to pH 11.

Materials Characterization. Bright field optical microscopy was performed using an Olympus BX51BD microscope. Raman imaging was obtained using the Ramantouch microspectrometer (Nanophoton Inc., Osaka, Japan) equipped with an Apochromat NIR water immersion objective from Nikon (60× magnification, NA 1.0). The wavelength and power of excitation laser were set at 532 nm and 0.10 mW, respectively, and Raman acquisition was performed with an exposure time of 0.8 s/line. All data for the physical characterization of BSA microstructures were averaged using at least 10 measurements.

Data Analysis. Measurements of swelling ratio, pH-induced changes in porosity of the transformative 2D arrays, and Voronoi analysis of as-fabricated BSA microstructures were conducted using ImageJ. The differences in array configurations were evaluated by recognizing and identifying the well-defined corners of polygons, as well as the center of individual microstructures, as reference points. Voronoi tessellation was employed to visually illustrate the change in array configurations. Since Voronoi tessellations change with "nodes" assignment, for consistency, reference "nodes" are allocated on the vertices and center of a triangular microstructure according to D_{3h} symmetry of a triangular prism (Figure S11a). On the other hand, we assign a single "node" at the center of these shape-shifted circular BSA microstructures to denote its $D_{\infty h}$ (Figure S11b). We would like to clarify that virtual networks generated using Voronoi tessellation varies with allocation of "nodes", which means other arbitrary choices of reference positions would produce different virtual network transformations.

Conflict of Interest: The authors declare no competing financial interest.

Acknowledgment. X.Y.L. is thankful for the support from National Research Foundation, Singapore (NRF-NRFF2012-04), and Nanyang Technological University's start-up grant (M4080758). C.L.L. and H.K.L. are thankful for the support from A*STAR Graduate Scholarship, Singapore. M.R.L. is thankful for the support from Nanyang Presidential Graduate Scholarship, Singapore.

Supporting Information Available: The Supporting Information is available free of charge on the ACS Publications website at DOI: 10.1021/acsnano.5b04300.

Details on swelling ratio against z-layer distance, dynamic geometrical shape-shifting of BSA microstructures, effect of frame designs on shape transformations, comparison on Voronoi tessellations of fabricated arrays with Kagome and open-structured hexagonal configurations with theoretical array configurations, array configuration transformations against pH, effect of skeletal frames to array configuration transformation, different types of unit cells of periodic 2D arrays. (PDF)

Movies of reversible circle-to-polygons, polygons-to-circle, Kagome-to-hexagonal configuration transition and open-structured hexagonal-to-percolating hexagonal configuration transformations. (ZIP)

REFERENCES AND NOTES

1. Brainerd, E. L. Pufferfish Inflation: Functional Morphology of Postcranial Structures in Diodon Holocanthus (Tetraodontiformes). *J. Morphol.* **1994**, *220*, 243–261.

2. Volkov, A. G.; Foster, J. C.; Ashby, T. A.; Walker, R. K.; Johnson, J. A.; Markin, V. S. Mimosa Pudica: Electrical and Mechanical Stimulation of Plant Movements. *Plant, Cell Environ.* **2010**, *33*, 163–173.
3. Shimaoka, M.; Xiao, T.; Liu, J.-H.; Yang, Y.; Dong, Y.; Jun, C.-D.; McCormack, A.; Zhang, R.; Joachimiak, A.; Takagi, J.; *et al.* Structures of the αL I Domain and Its Complex with ICAM-1 Reveal a Shape-Shifting Pathway for Integrin Regulation. *Cell* **2003**, *112*, 99–111.
4. Studart, A. R.; Erb, R. M. Bioinspired Materials that Self-Shape Through Programmed Microstructures. *Soft Matter* **2014**, *10*, 1284–1294.
5. Landau, J. V. High Hydrostatic Pressure Effects on Amoeba Proteus Changes in Shape, Volume, and Surface Area. *J. Cell Biol.* **1965**, *24*, 332–336.
6. Wang, Y.; Wang, Y.; Breed, D. R.; Manoharan, V. N.; Feng, L.; Hollingsworth, A. D.; Weck, M.; Pine, D. J. Colloids with Valence and Specific Directional Bonding. *Nature* **2012**, *491*, 51–55.
7. Yoo, J.-W.; Mitragotri, S. Polymer Particles that Switch Shape in Response to a Stimulus. *Proc. Natl. Acad. Sci. U. S. A.* **2010**, *107*, 11205–11210.
8. Rahmani, S.; Saha, S.; Durmaz, H.; Donini, A.; Misra, A. C.; Yoon, J.; Lahann, J. Chemically Orthogonal Three-Patch Microparticles. *Angew. Chem.* **2014**, *126*, 2364–2370.
9. Ionov, L. Hydrogel-based Actuators: Possibilities and Limitations. *Mater. Today* **2014**, *17*, 494–503.
10. Yang, Z.; Huck, W. T. S.; Clarke, S. M.; Tajbakhsh, A. R.; Terentjev, E. M. Shape-Memory Nanoparticles from Inherently Non-Spherical Polymer Colloids. *Nat. Mater.* **2005**, *4*, 486–490.
11. Kohlmeyer, R. R.; Buskohl, P. R.; Deneault, J. R.; Durstock, M. F.; Vaia, R. A.; Chen, J. Shape-Reprogrammable Polymers: Encoding, Erasing, and Re-Encoding. *Adv. Mater.* **2014**, *26*, 8114–8119.
12. Lee, J. B.; Peng, S.; Yang, D.; Roh, Y. H.; Funabashi, H.; Park, N.; Rice, E. J.; Chen, L.; Long, R.; Wu, M.; *et al.* A Mechanical Metamaterial Made from a DNA Hydrogel. *Nat. Nanotechnol.* **2012**, *7*, 816–820.
13. Ma, C.; Li, T.; Zhao, Q.; Yang, X.; Wu, J.; Luo, Y.; Xie, T. Supramolecular Lego Assembly towards Three-Dimensional Multi-Responsive Hydrogels. *Adv. Mater.* **2014**, *26*, 5665–5669.
14. Kozlovskaya, V.; Higgins, W.; Chen, J.; Kharlampieva, E. Switching Shape of Hollow Layer-by-Layer Hydrogel Microcontainers. *Chem. Commun.* **2011**, *47*, 8352–8354.
15. Palleau, E.; Morales, D.; Dickey, M. D.; Velev, O. D. Reversible Patterning and Actuation of Hydrogels by Electrically Assisted Ionoprinting. *Nat. Commun.* **2013**, *4*, 2257.
16. Malachowski, K.; Jamal, M.; Jin, Q.; Polat, B.; Morris, C. J.; Gracias, D. H. Self-Folding Single Cell Grippers. *Nano Lett.* **2014**, *14*, 4164–4170.
17. Xiong, Z.; Zheng, M.-L.; Dong, X.-Z.; Chen, W.-Q.; Jin, F.; Zhao, Z.-S.; Duan, X.-M. Asymmetric Microstructure of Hydrogel: Two-Photon Microfabrication and Stimuli-Responsive Behavior. *Soft Matter* **2011**, *7*, 10353–10359.
18. Song, S. H.; Park, J. H.; Chitnis, G.; Siegel, R. A.; Ziaie, B. A Wireless Chemical Sensor Featuring Iron Oxide Nanoparticle-Embedded Hydrogels. *Sens. Actuators, B* **2014**, *193*, 925–930.
19. Wu, Z. L.; Moshe, M.; Greener, J.; Therien-Aubin, H.; Nie, Z.; Sharon, E.; Kumacheva, E. Three-Dimensional Shape Transformations of Hydrogel Sheets Induced by Small-Scale Modulation of Internal Stresses. *Nat. Commun.* **2013**, *4*, 1586.
20. Bai, T.; Han, Y.; Zhang, P.; Wang, W.; Liu, W. Zinc Ion-Triggered Two-Way Macro-/Microscopic Shape Changing and Memory Effects in High Strength Hydrogels with Pre-Programmed Unilateral Patterned Surfaces. *Soft Matter* **2012**, *8*, 6846–6852.
21. Yang, Q.; Adrus, N.; Tomicki, F.; Ulbricht, M. Composites of Functional Polymeric Hydrogels and Porous Membranes. *J. Mater. Chem.* **2011**, *21*, 2783–2811.
22. Amini, H.; Lee, W.; Di Carlo, D. Inertial Microfluidic Physics. *Lab Chip* **2014**, *14*, 2739–2761.
23. Kieviet, B. D.; Schon, P. M.; Vancso, G. J. Stimulus-Responsive Polymers and other Functional Polymer Surfaces as Components in Glass Microfluidic Channels. *Lab Chip* **2014**, *14*, 4159–4170.
24. Nguyen, T. D.; Jankowski, E.; Glotzer, S. C. Self-Assembly and Reconfigurability of Shape-Shifting Particles. *ACS Nano* **2011**, *5*, 8892–8903.
25. Nguyen, T. D.; Glotzer, S. C. Reconfigurable Assemblies of Shape-Changing Nanorods. *ACS Nano* **2010**, *4*, 2585–2594.
26. Dick, K. A.; Caroff, P.; Bolinsson, J.; Messing, M. E.; Johansson, J.; Deppert, K.; Wallenberg, L. R.; Samuelson, L. Control of III−V Nanowire Crystal Structure by Growth Parameter Tuning. *Semicond. Sci. Technol.* **2010**, *25*, 024009.
27. Cobb, A. B. *The Basics of Nonmetals*; Rosen Publishing Group, Inc.: New York, 2013.
28. Ge, J.; Yin, Y. Responsive Photonic Crystals. *Angew. Chem., Int. Ed.* **2011**, *50*, 1492–1522.
29. Yin, S.-N.; Wang, C.-F.; Liu, S.-S.; Chen, S. Facile Fabrication of Tunable Colloidal Photonic Crystal Hydrogel Supraballs toward a Colorimetric Humidity Sensor. *J. Mater. Chem. C* **2013**, *1*, 4685–4690.
30. Marcombe, R.; Cai, S.; Hong, W.; Zhao, X.; Lapusta, Y.; Suo, Z. A Theory of Constrained Swelling of a pH-Sensitive Hydrogel. *Soft Matter* **2010**, *6*, 784–793.
31. Silverberg, J. L.; Evans, A. A.; McLeod, L.; Hayward, R. C.; Hull, T.; Santangelo, C. D.; Cohen, I. Using Origami Design Principles to Fold Reprogrammable Mechanical Metamaterials. *Science* **2014**, *345*, 647–650.
32. Kim, J.; Hanna, J. A.; Byun, M.; Santangelo, C. D.; Hayward, R. C. Designing Responsive Buckled Surfaces by Halftone Gel Lithography. *Science* **2012**, *335*, 1201–1205.
33. Lee, M. R.; Phang, I. Y.; Cui, Y.; Lee, Y. H.; Ling, X. Y. Shape-Shifting 3D Protein Microstructures with Programmable Directionality *via* Quantitative Nanoscale Stiffness Modulation. *Small* **2015**, *11*, 740–748.
34. Spivey, E. C.; Ritschdorff, E. T.; Connell, J. L.; McLennon, C. A.; Schmidt, C. E.; Shear, J. B. Multiphoton Lithography of Unconstrained Three-Dimensional Protein Microstructures. *Adv. Funct. Mater.* **2013**, *23*, 333–339.
35. Kawata, S.; Sun, H.-B.; Tanaka, T.; Takada, K. Finer Features for Functional Microdevices. *Nature* **2001**, *412*, 697–698.
36. Ritschdorff, E. T.; Nielson, R.; Shear, J. B. Multi-Focal Multiphoton Lithography. *Lab Chip* **2012**, *12*, 867–71.
37. Salis, A.; Boström, M.; Medda, L.; Cugia, F.; Barse, B.; Parsons, D. F.; Ninham, B. W.; Monduzzi, M. Measurements and Theoretical Interpretation of Points of Zero Charge/Potential of BSA Protein. *Langmuir* **2011**, *27*, 11597–11604.
38. Katifori, E.; Alben, S.; Cerda, E.; Nelson, D. R.; Dumais, J. Foldable Structures and The Natural Design of Pollen Grains. *Proc. Natl. Acad. Sci. U. S. A.* **2010**, *107*, 7635–7639.
39. Vedmedenko, E. *Competing Interactions and Pattern Formation in Nanoworld*; Wiley-VCH: Weinheim, 2007; Vol. 1, p 215.
40. Xie, S.-Y.; Li, X.-B.; Tian, W. Q.; Chen, N.-K.; Wang, Y.; Zhang, S.; Sun, H.-B. A Novel Two-Dimensional MgB_6 Crystal: Metal-Layer Stabilized Boron Kagome Lattice. *Phys. Chem. Chem. Phys.* **2015**, *17*, 1093–1098.
41. Rougemaille, N.; Montaigne, F.; Canals, B.; Duluard, A.; Lacour, D.; Hehn, M.; Belkhou, R.; Fruchart, O.; El Moussaoui, S.; Bendounan, A.; *et al.* Artificial Kagome Arrays of Nanomagnets: A Frozen Dipolar Spin Ice. *Phys. Rev. Lett.* **2011**, *106*, 057209.
42. Hoai Nguyen, H.; Gunnar, P.; Lock Yue, C. The Abelian Manna Model on Various Lattices in One and Two Dimensions. *J. Stat. Mech.: Theory Exp.* **2011**, *2011*, P09024.
43. Okabe, A.; Boots, B.; Sugihara, K.; Chiu, S. N. *Spatial Tessellations: Concepts and Applications of Voronoi Diagrams*; Wiley: New York, 2009.
44. Yazdchi, K.; Srivastava, S.; Luding, S. Microstructural Effects on The Permeability of Periodic Fibrous Porous Media. *Int. J. Multiphase Flow* **2011**, *37*, 956–966.
45. Chenwei, L.; Joong Yull, P.; Yugong, X.; SangHoon, L. Arrayed pH-Responsive Microvalves Controlled by Multiphase Laminar Flow. *J. Micromech. Microeng.* **2007**, *17*, 1985.
46. Liu, R. H.; Bonanno, J.; Yang, J.; Lenigk, R.; Grodzinski, P. Single-Use, Thermally Actuated Paraffin Valves for Microfluidic Applications. *Sens. Actuators, B* **2004**, *98*, 328–336.